Supplementary information (SI) for

Barrier-Thickness-Engineered Giant Magnetotransport and Multi-Level Storage in a $CrTe_2/Al_2S_3$ Van der Waals Multiferroic Junction

Yunlai Zhu [a], Ke Wang [a], Chaotong Xie [a], Tao Jiang [a], Yong Zhang [a], Zhongren Ye [a], Xiaoling Wu [a], Haotian Tang [a], Xi Sun [a], Tong Zhu [a], Zuyu Xu [a], Zhe Feng [a], Lihua Xu [a], Wendong Lu [a], Zuheng Wu [a*], Yuehua Dai [a*]

[a] School of Integrated Circuits, Anhui University, Hefei, Anhui, 230601, China.

Corresponding Authors

*E-mail: wuzuheng@ahu.edu.cn (Z.-H. Wu), daiyuehua@ahu.edu.cn (Y.-H. Dai)

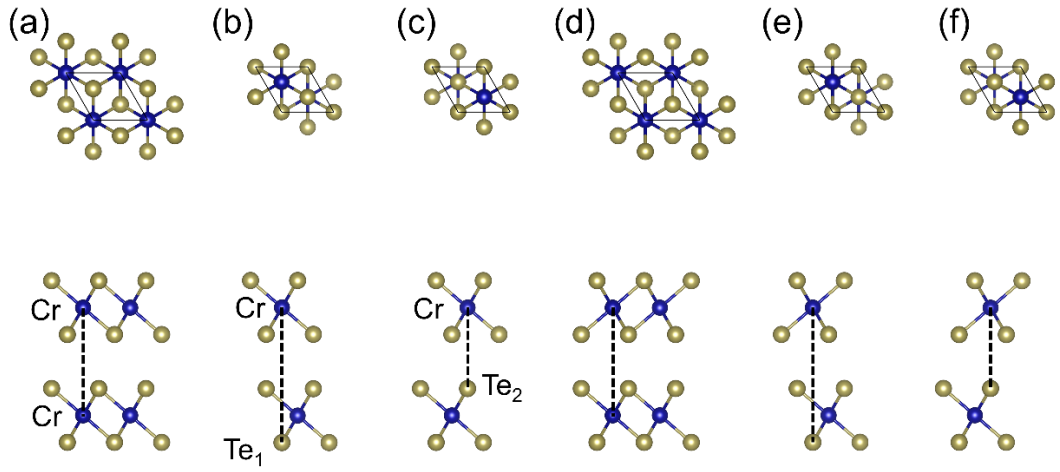

Fig. S1 The different stacking configurations of bilayer $CrTe_2$. (a)-(f) shows the AA, AB, AC, A'A, A'B, A'C state, respectively.

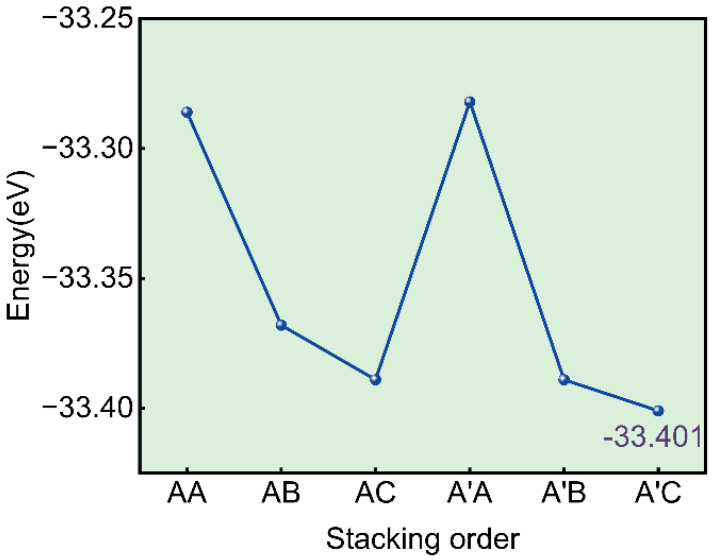

Fig. S2 The energies corresponding to the six stacking structures of bilayer $CrTe_2$.

Using the linear response method, we systematically scanned Hubbard U values from 1.0 to 9.0 eV in equal increments; the corresponding electronic band structures are shown in **Fig. S3**. $CrTe_2$ exhibits metallic ferromagnetic behavior across the entire U range, characterized by pronounced spin splitting in the density of states and the absence of a band gap. Notably, as U increases, the bands near the Γ and M points shift upward progressively, reflecting enhanced localization of the Cr 3d electrons. By comparing with previous studies and our own computational validation,[1, 2] $U = 2$ eV is determined as the rational parameter for accurately describing the band structure of $CrTe_2$.

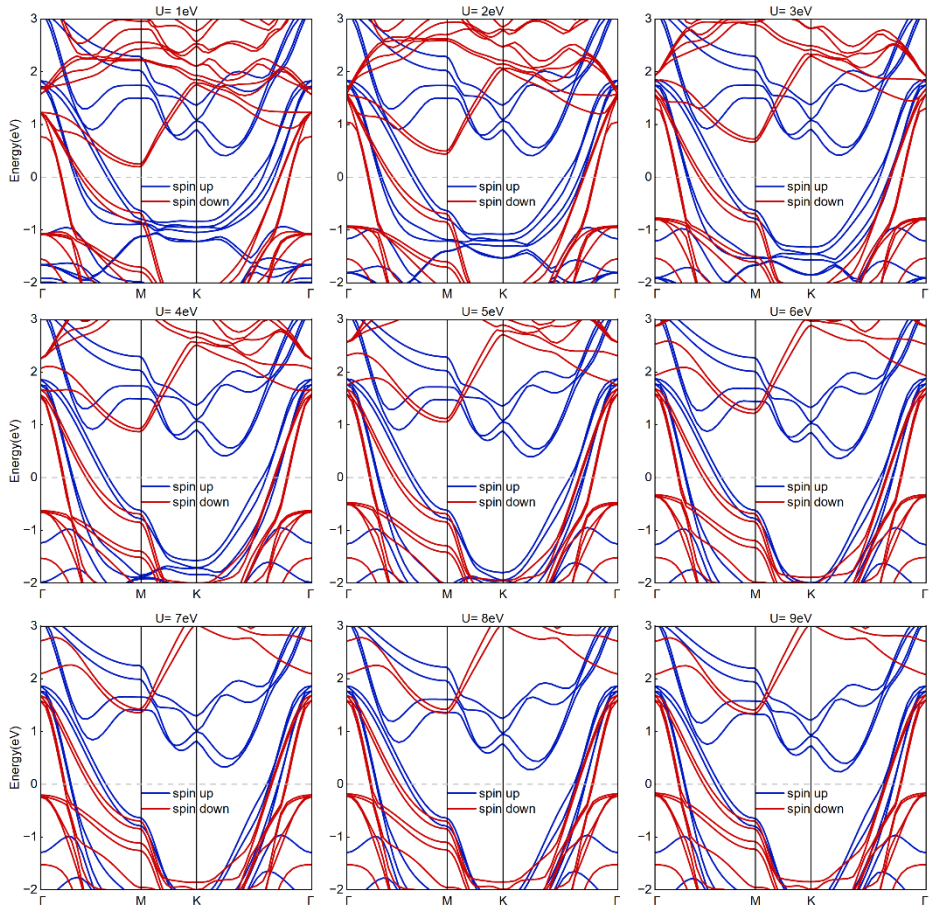

Fig. S3 Band structures of $CrTe_2$ at *U* values ranging from 1 to 9 eV.

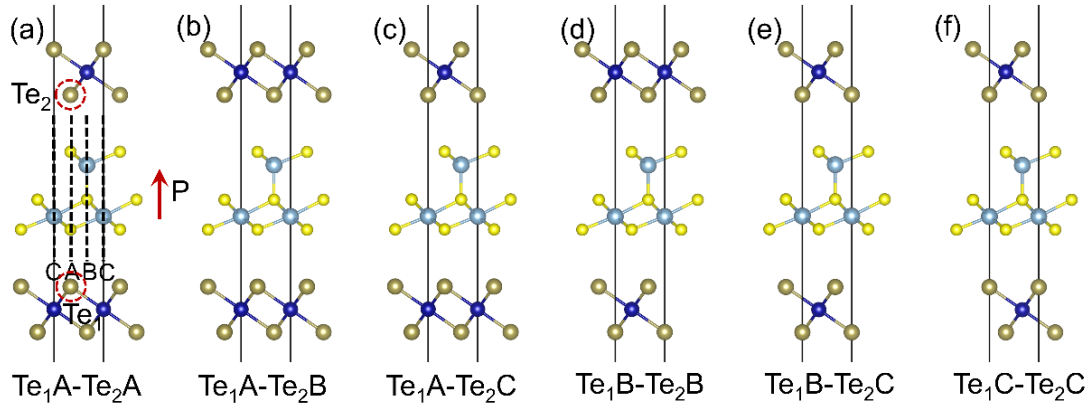

Fig. S4 The six stacking structures of the single-layer Al_2S_3 barrier with upward polarization.

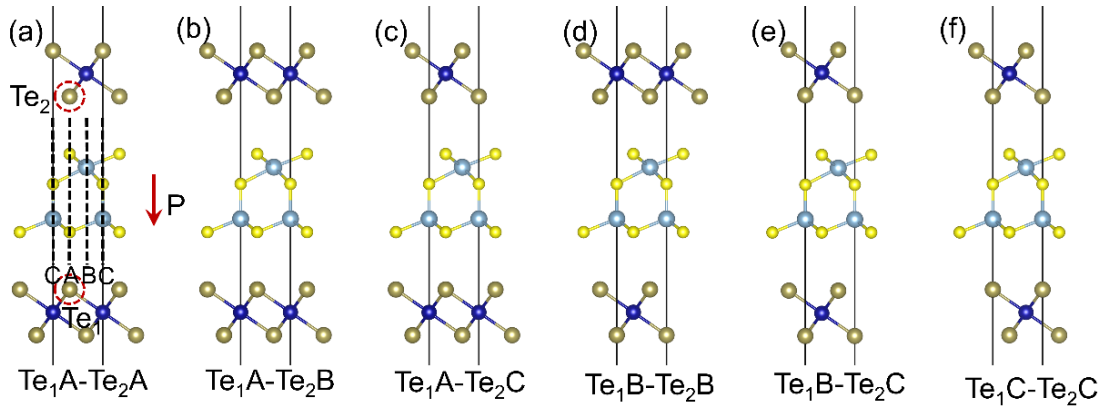

Fig. S5 The six stacking structures of the single-layer Al_2S_3 barrier with downward polarization.

The binding energy of the monolayer $Al_2S_3/CrTe_2$ heterojunction by calculating its binding energy has been evaluated. The calculation formula for binding energy is given as follows:[3]

$$E_b = \frac{E_{hetero} - (E_{Al_2S_3} + E_{up-CrTe_2} + E_{\mathrm{down-CrTe_2}})}{A}$$

Where E_{hetero} is the total energy of the optimized $Al_2S_3/CrTe_2$ heterojunction. $E_{Al_2S_3}$, $E_{up-CrTe_2}$ and $E_{down-CrTe_2}$ are the energies of the isolated, optimized monolayer Al_2S_3 and the upper and lower $CrTe_2$ electrodes, respectively, and A is the interfacial area. Calculations across all twelve stacking configurations yield negative E_b values (**Table S1**), confirming thermodynamic stability. Among these, the $Te_1B–Te_2C$ stacking is the most stable for upward polarization, while $Te_1C–Te_2C$ stacking is most stable for downward polarization.

Table. S1 Binding energies of monolayer $Al_2S_3/CrTe_2$ heterojunctions with different stacking configurations. (unit: $meV/Å^2$)

Polarization direction	Stacking configuration	E_b
UP	Te_1A-Te_2A	-212.7
	Te_1A-Te_2B	-218.1
	Te_1A-Te_2C	-218.8
	Te_1B-Te_2B	-224.7
	Te_1B-Te_2C	-225.3
	Te_1C-Te_2C	-224.4
Down	Te_1A-Te_2A	-212.7
	Te_1A-Te_2B	-218.1
	Te_1A-Te_2C	-211.6
	Te_1B-Te_2B	-217.9
	Te_1B-Te_2C	-217.9
	Te_1C-Te_2C	-224.7

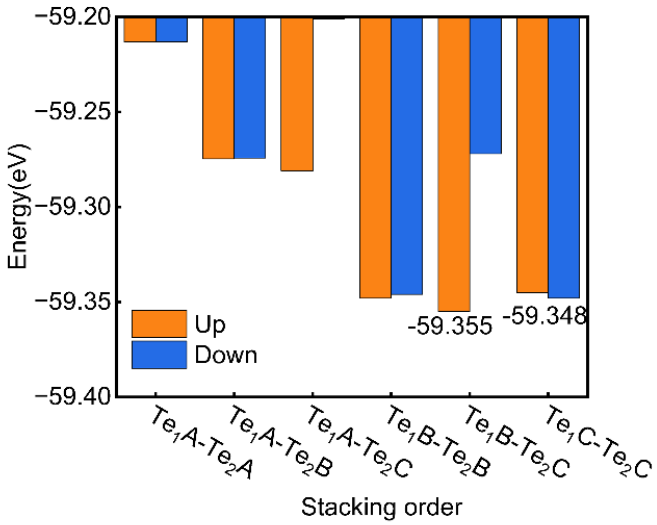

Fig. S6 The energies under the twelve stacking structures of the single-layer Al_2S_3 barrier.

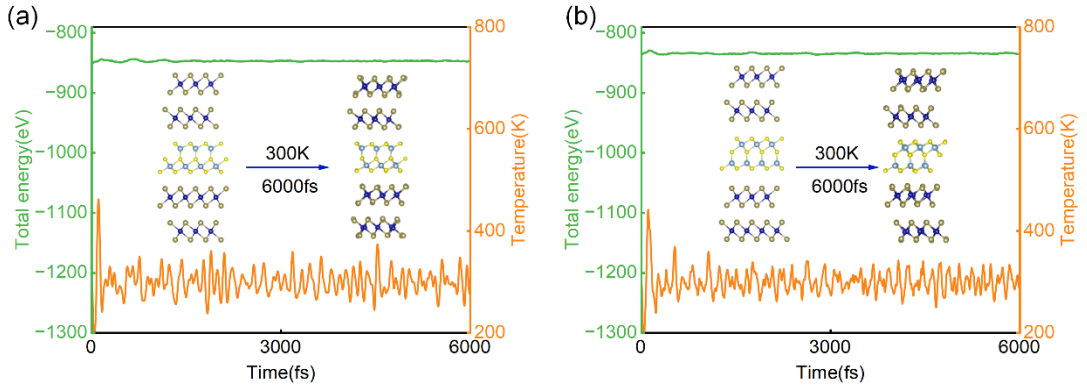

Fig. S7 AIMD simulations at 300 K for the (a) polarization-up and (b) polarization-down configurations. Plots show the evolution of total energy and temperature over time; structural snapshots at 6 ps confirm that both configurations remain stable without phase transformation.

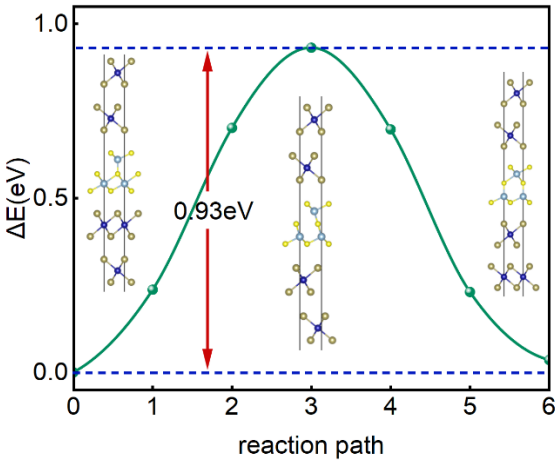

Fig. S8 Total-energy profile along the polarization-switching path between the FE-R and FE-L states in monolayer Al_2S_3 placed between bilayer $CrTe_2$ electrodes. The reaction coordinates 0 and 6 correspond to the FE-R and FE-L states, respectively.

We explored the multiple polarization configurations available in bilayer Al_2S_3: ferroelectric (FE, with both layers polarized in the same direction), head-to-head anti-ferroelectric (AFE-Head), and tail-to-tail anti-ferroelectric (AFE-Tail). However, in a symmetric CT/BAS/CT junction, the two uniform FE states (FE-R and FE-L) are functionally equivalent due to identical interfacial band offsets, resulting in a negligible TER ratio unsuitable for device operation.[4] Consequently, we excluded the FE-L state and focused on the three distinct dipole configurations illustrated in **Fig. S9(a)**: FE, AFE-Tail, and AFE-Head.

The structural stability of these states is highly dependent on the interlayer stacking registry. For each polarization state, we considered three stacking configurations (S-A, S-B, S-C), defined by the relative position of the top sulfur atom with respect to the bottom-layer atoms. After sufficient lattice relaxation, our calculations (**Fig. S9(b)**) identified the S-C stacking as the most stable for the FE and AFE-Tail states, and the S-B stacking for the AFE-Head state. Subsequent device modeling employed these optimal stacking geometries.

The electronic band structures of the three selected states are presented in **Figs. S9(c)-(e)**. All configurations exhibit an indirect bandgap, with the two AFE states possessing larger gaps than the FE state—a difference arising from the depolarization electric field induced by the net out-of-plane polarization in the FE state. The semiconducting character of all three states confirms the suitability of double-layer Al_2S_3 as a tunnel barrier. We therefore constructed three distinct van der Waals MFTJs (CT/BAS/CT), each corresponding to one of these stable ferroelectric configurations.

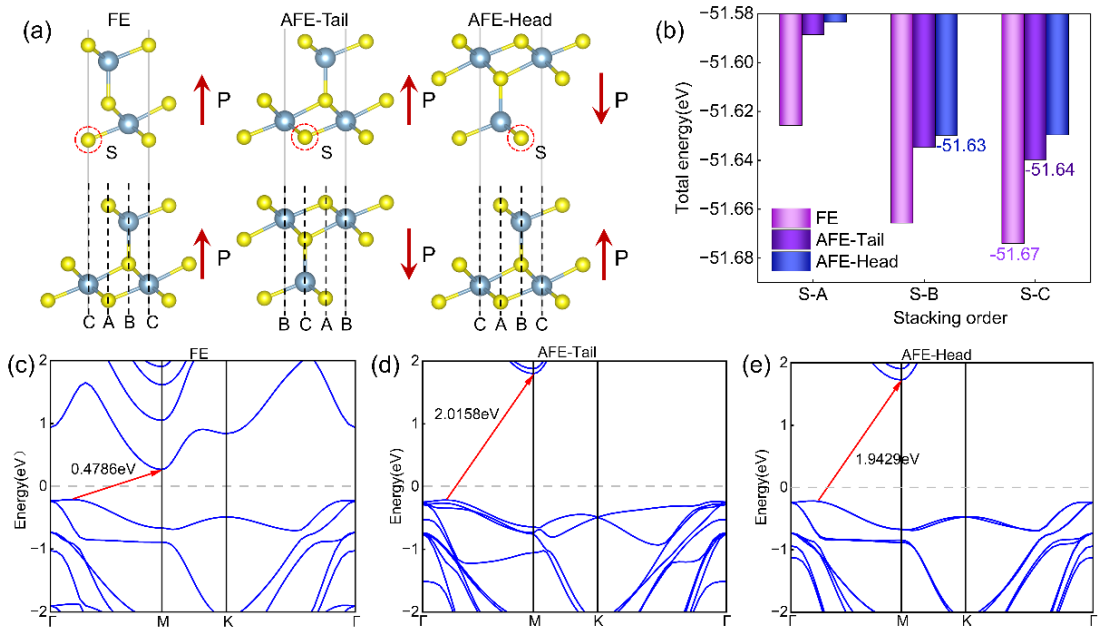

Fig. S9 (a) Illustration of the atomic arrangements in bilayer Al_2S_3 corresponding to three unique ferroelectric polarization directions (marked by red arrows), which are the FE, AFE-Tail, and AFE-Head states. (b) Plot of the total energy of bilayer Al_2S_3 for the three polarization states at different stacking arrangements. Band structures of bilayer Al_2S_3 in the FE (c), AFE-Tail (d), and AFE-Head (e) states, where the Fermi level is aligned at zero energy.

To identify the optimal interface configuration for the MFTJ, we explored different stacking registries by laterally shifting the electrodes. For the symmetric junction, six unique stacking sequences were considered: Te1(A)-Te2(A), Te1(A)-Te2(B), Te1(A)-Te2(C), Te1(B)-Te2(B), Te1(B)-Te2(C), and Te1(C)-Te2(C).[5, 6] Accounting for the three ferroelectric states, this resulted in a total of eighteen possible configurations (**Figs. S10-S12**). The total energy evaluations (**Fig. S13**) reveal that the Te1(B)-Te2(C) stacking is the most stable for the FE and AFE-Head states, while the Te1(B)-Te2(B) stacking is most favorable for the AFE-Tail state.

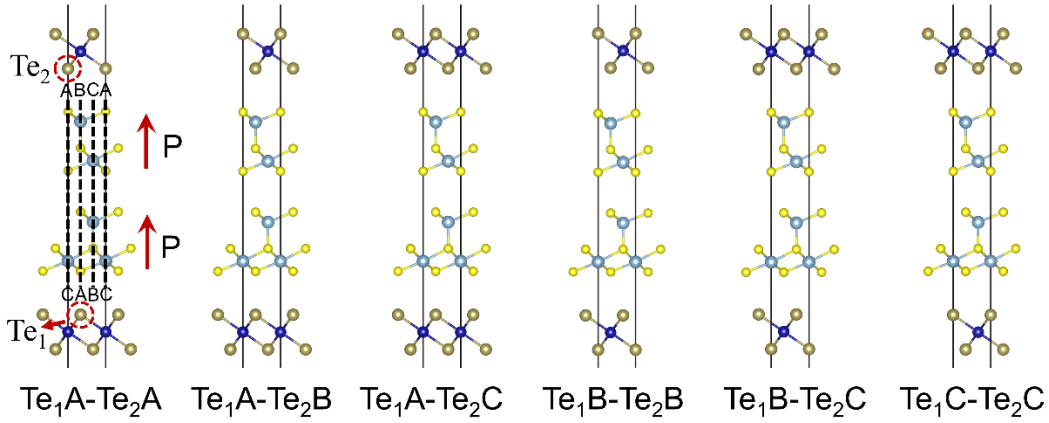

Fig. S10 The six stacking structures of the bilayer Al_2S_3 barrier with double upward polarization.

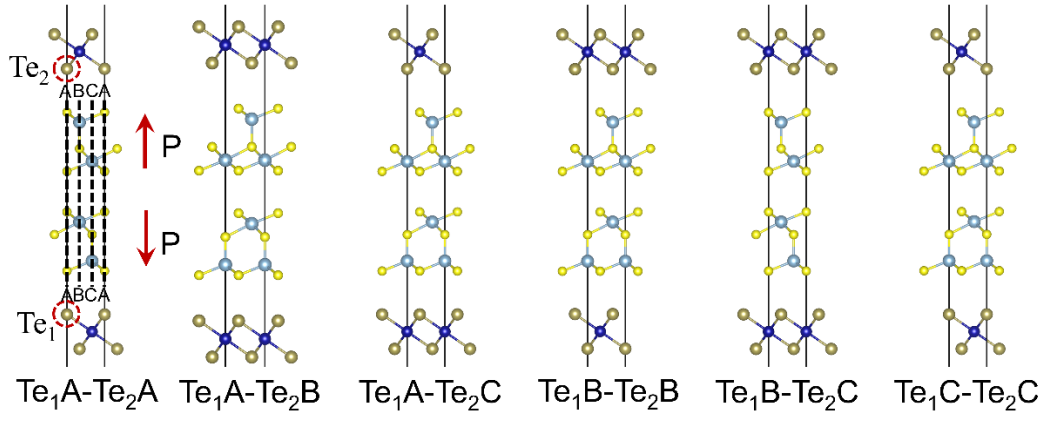

Fig. S11 The six stacking structures of the bilayer Al_2S_3 barrier with tail polarization.

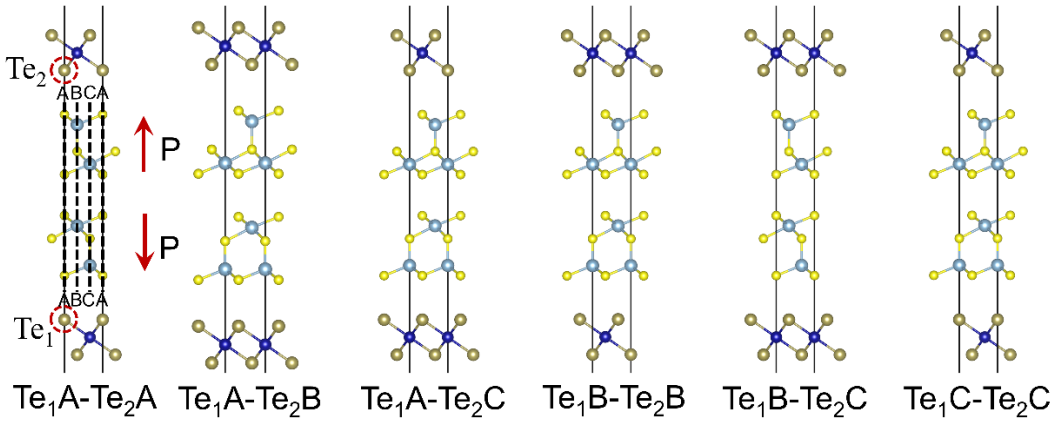

Fig. S12 The six stacking structures of the bilayer Al_2S_3 barrier with head polarization.

Based on the binding energy calculations of the monolayer $Al_2S_3/CrTe_2$ heterostructure, the binding energy analysis of the bilayer system was further carried out. By comparing the binding energies of three different polarization states under six stacking configurations, the results indicate that the most stable stacking mode for FE and AFE-Head is Te_1B-Te_2C, whereas AFE-Tail is most stable in the Te_1B-Te_2B stacking (**Table. S2**).

Table. S2 Binding energies of bilayer $Al_2S_3/CrTe_2$ heterojunctions with different stacking configurations. (unit: $meV/Å^2$)

Polarization direction	Stacking configuration	E_b
FE	Te_1A-Te_2A	-213.8
	Te_1A-Te_2B	-220.1
	Te_1A-Te_2C	-220.7
	Te_1B-Te_2B	-227.2
	Te_1B-Te_2C	-229.3
	Te_1C-Te_2C	-227.1
AFE-Tail	Te_1A-Te_2A	-202.7
	Te_1A-Te_2B	-207.7
	Te_1A-Te_2C	-208.1
	Te_1B-Te_2B	-213.1
	Te_1B-Te_2C	-206.2
	Te_1C-Te_2C	-205.7
AFE-Head	Te_1A-Te_2A	-198.7
	Te_1A-Te_2B	-211.4
	Te_1A-Te_2C	-212.2
	Te_1B-Te_2B	-217.6
	Te_1B-Te_2C	-218.4
	Te_1C-Te_2C	-217.6

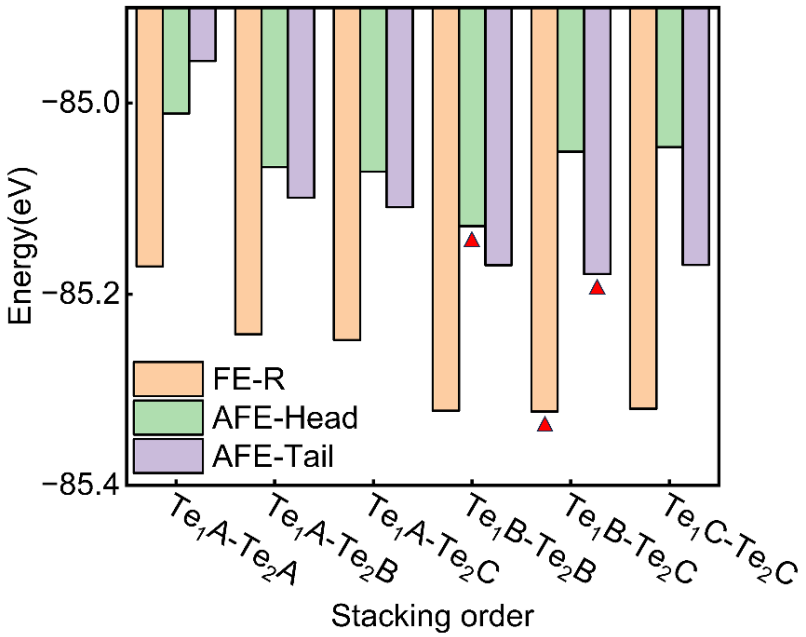

Fig. S13 The energies under the eighteen stacking structures of the bilayer Al_2S_3 barrier. The red triangles represent the lowest energy of stacking.

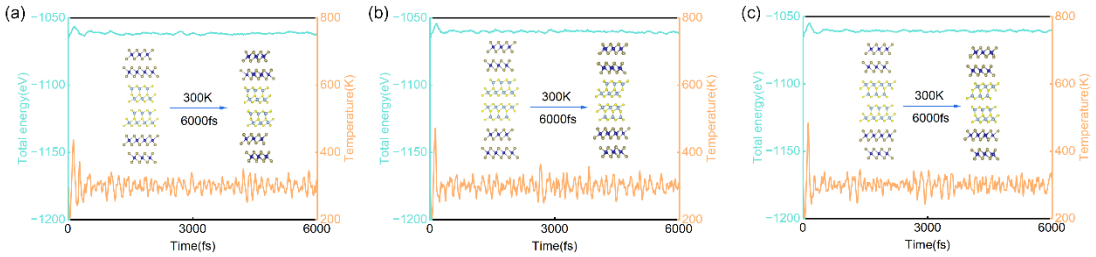

Fig. S14 AIMD simulations at 300 K for the bilayer Al_2S_3 barrier in the (a) FE, (b) AFE-Tail, and (c) AFE-Head states. Total energy and temperature are plotted versus time; final snapshots (6 ps) demonstrate structural stability with no phase transition.

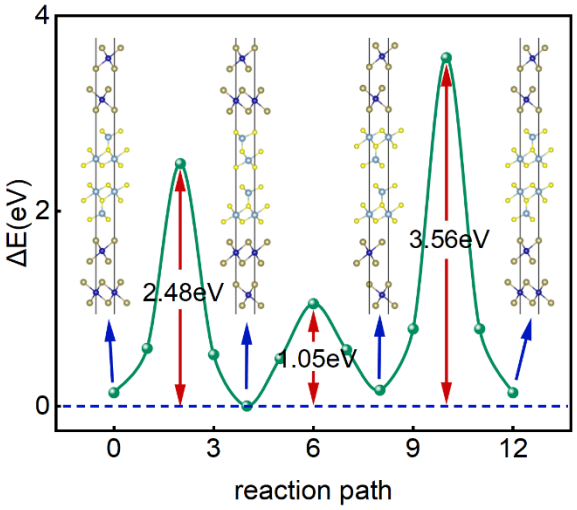

Fig. S15 Total-energy profiles for polarization switching between the three stable states (AFE-Tail, FE, and AFE-Head) in bilayer Al_2S_3. The reaction coordinates 0, 4, 8, and 12 denote the AFE-Tail → FE → AFE-Head → AFE-Tail transition pathway.

Fig. S16 presents the spin-dependent Layer-Projected Density of States (LPDOS) for the CT/BAS/CT structure. The bilayer $CrTe_2$ electrodes exhibit pronounced metallic character, as evidenced by their significant LPDOS at E_f. Consequently, the spin-polarized electron transport is primarily governed by the electronic structure of the ferroelectric bilayer Al_2S_3 barrier.[7] In the ferroelectric (FE) state (**Figs. S16(a)** and **(b)**), the PDOS of the bilayer Al_2S_3 shows no significant features near E_f, with the closest peaks situated at a considerable energy separation. This large separation creates a high tunnel barrier, rationalizing the lowest transmission coefficient observed for this state. Conversely, in the antiferroelectric-tail (AFE-tail) state ((**Figs. S16(c)** and **(d)**), the PDOS peaks shift closer to E_f, reducing the effective barrier height and resulting in enhanced transmission. Most notably, the antiferroelectric-head (AFE-head) state—which exhibits the maximum transmission—is characterized by sharp PDOS peaks immediately adjacent to E_f (**Figs. S16(e)** and **(f)**), indicating a substantially lowered tunnel barrier. The strong correlation between the energy alignment of the bilayer Al_2S_3 PDOS features with E_f a and the computed transmission coefficients across all ferroelectric phases validates our LPDOS analysis.

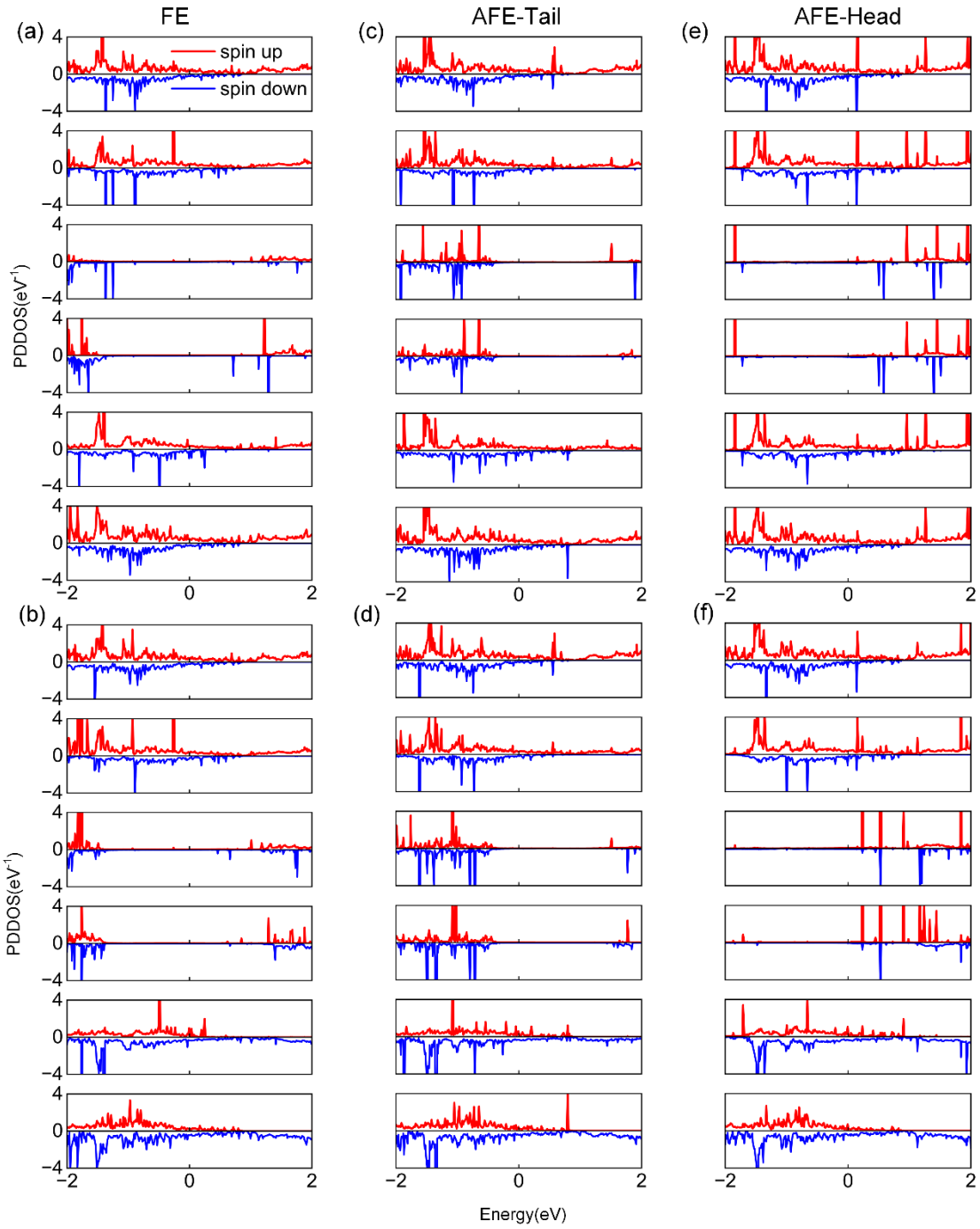

Fig. S16 Spin-resolved and layer-resolved Projected Device Density of States (LPDOS) of the MFTJ under different magnetic and ferroelectric configurations. For the CT/BAS/CT structure: (a) FE PC; (b) FE APC; (c)AFE-Tail PC; (d) AFE-Tail APC; (e) AFE-Head PC; (f) AFE-Head APC.

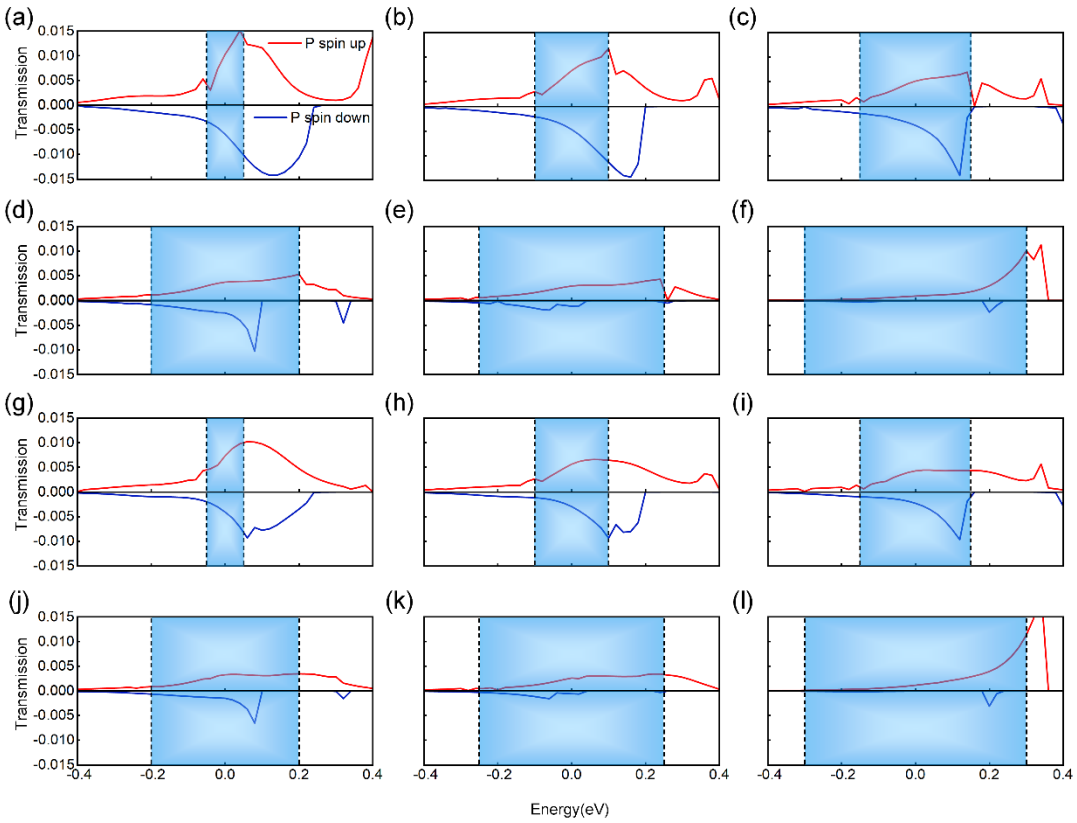

Fig. S17 Spin-resolved transmission spectra of the CT/BAS/CT van der Waals MFTJ under bias voltages from 0.1 to 0.6 V for the AFE-Head state with parallel magnetization. The blue shaded rectangle indicates the bias window used for current integration; the Fermi level is set to 0 eV. Panels (a)–(f) correspond to the parallel configuration at 0.1–0.6 V; panels (g)–(l) show the antiparallel configuration over the same bias range. Positive values (red curves) represent spin-up transmission; negative values (blue curves) represent spin-down transmission.

To examine the impact of defects in the proposed heterostructure, we focus on vacancy defects as the primary perturbation. Introducing S or Te vacancies into the ferroelectric Al_2S_3 barrier directly induces structural distortion, leading to significant asymmetry in both the height and morphology of the barrier under different polarization configurations. More importantly, such vacancies alter the interfacial work function and break the symmetry of the bilayer's polarization-switching pathway, making the FE-R and FE-L states non-equivalent and thereby generating an intrinsic TER signal.[8, 9] Based on this analysis, we systematically computed the electron transport properties for eight distinct magnetoelectric configurations with S or Te vacancies in the barrier. The corresponding device schematics and detailed data are provided in **Figs. S18** and **S19**

and **Tables S3** and **S4**.

For the S-vacancy system (defect positions shown in **Fig. S18**), the device performance degrades moderately: the maximum TER drops from 3912.0% (pristine) to 1190.5%, and the maximum TMR decreases from 124.7% to 104.5% (**Table S3**). Similarly, introducing Te vacancies (positions in **Fig. S19**) reduces the maximum achievable TER and TMR to 2294.2% and 118.8%, respectively (**Table S4**). Despite this reduction, the performance remains substantially higher than that of the pristine monolayer barrier system, confirming that the strategy of increasing barrier thickness effectively enhances both TER and TMR. Notably, the introduction of S vacancies increases the number of distinguishable conductive configurations from six to eight, effectively expanding the count of non-volatile memory states and further demonstrating the potential of this approach to improve storage density.

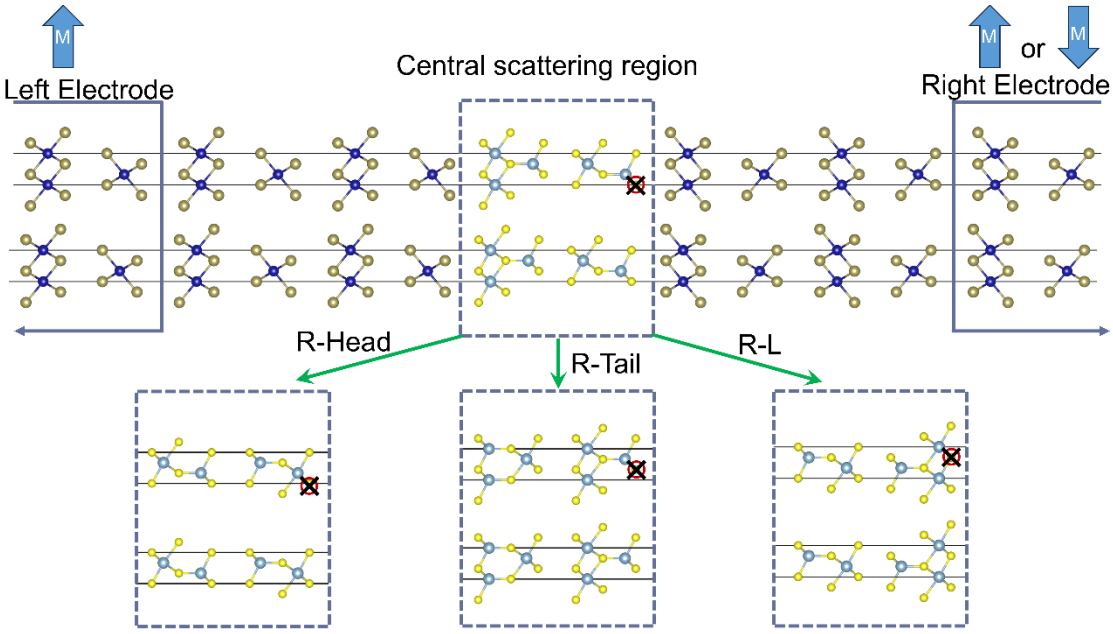

Fig. S18 Schematic of the defective MFTJ device with an S vacancy (marked by a red circle and cross) in the four polarization states: FE-R, AFE-Tail, AFE-Head, and FE-L.

Table. S3 Calculated transmission coefficients (unit: e^2/h), TMR and TER ratios of the MFTJ with an S vacancy in the FE-R, AFE-Tail, AFE-Head and FE-L states.

MFTJ	P state(M↑↑)	AP state(M↑↓)	TMR
	Total	Total	
FE(R)	3.97×10^{-4}	3.83×10^{-4}	3.6%
AFE-Tail	1.54×10^{-3}	7.54×10^{-4}	104.5%
AFE-Head	9.95×10^{-3}	9.07×10^{-3}	2.5%
FE(L)	6.88×10^{-4}	6.29×10^{-4}	9.3%
	287.7%	96.4%	
TER	2406.2%	2268.1%	
	73.1%	64.0%	

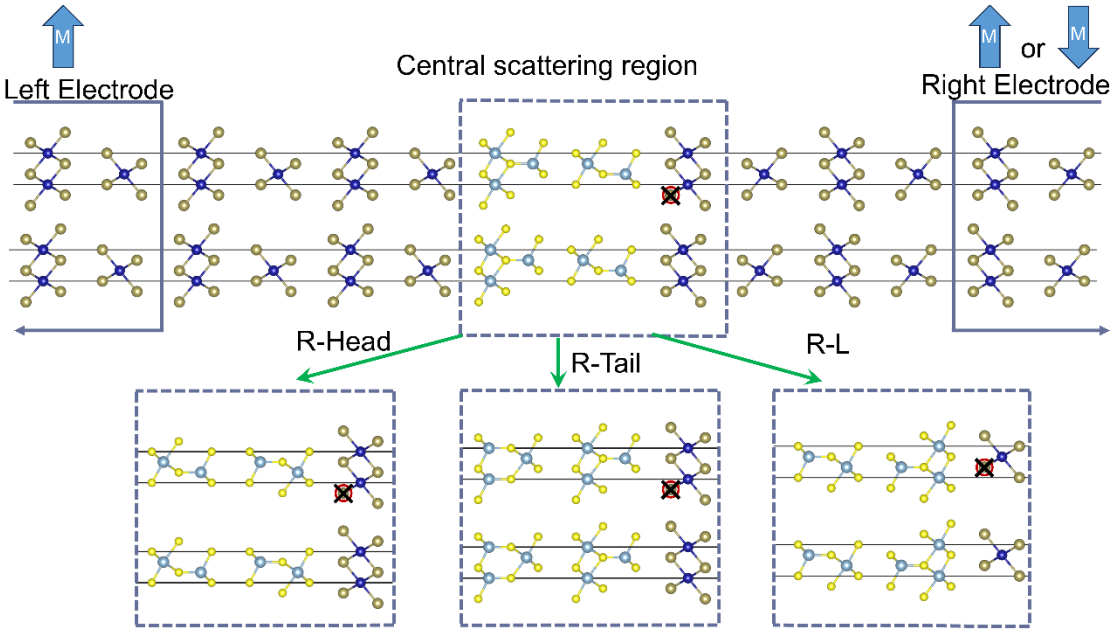

Fig. S19 Schematic of the defective MFTJ device with a Te vacancy (marked by a red circle and cross) in the four polarization states: FE-R, AFE-Tail, AFE-Head, and FE-L.

Table. S4 Calculated transmission coefficients (unit: e^2/h), TMR and TER ratios for the MFTJ a Te vacancy in the FE-R, AFE-Tail, AFE-Head and FE-L states.

MFTJ	P state(M↑↑)	AP state(M↑↓)	TMR
	Total	Total	
FE(R)	1.04×10^{-3}	9.90×10^{-4}	5.0%
AFE-Tail	4.64×10^{-3}	2.12×10^{-3}	118.8%
AFE-Head	2.49×10^{-2}	2.10×10^{-2}	18.5%
FE(L)	1.84×10^{-3}	1.53×10^{-3}	20.2%
	346.1%	114.1%	
TER	2294.2%	2021.2%	
	76.9%	54.5%	

Table. S5 The number of resistance states and the evaluated TMR and TER ratios based on In_2Se_3, h-BN and $CuInP_2S_6$ designs of MFTJs.

MFTJs	*TER*	*TMR*	*resistance states*	*Reference*
$PtTe_2/Fe_3GeTe_2$/monolayer α-$In_2Se_3/Fe_3GeTe_2/PtTe_2$	62%	89%	2	[10]
$CrSb/In_2Se_3/Fe_3GaTe_2$	707%	2308%	*	[7]
Fe_3GeTe_2/bilayer In_2Se_3/Fe_3GeTe_2	744%	1.1×10^7 %	6	[5]
$TiTe_2/MnSe_2/In_2S_3/MnSe_2/TiTe_2$	1771%	5698%	4	[11]
Fe_3GaTe_2/bilayer In_2Se_3/Fe_3GaTe_2	7600%	6.8×10^5 %	6	[12]
Fe_3GeTe_2/h-BN/bilayer In_2Se_3/h-BN/Fe_3GeTe_2	1.0×10^4 %	695%	4	[13]
$CrSe_2/CuInP_2S_6/CrSe_2$	90%	121%	2	[14]
Fe_3GeTe_2/graphene/bilayer-h-BN/graphene/CrI_3	1204%	193%	2	[15]
$CrTe_2$/bilayer$Al_2S_3/CrTe_2$	3912%	124.7%	6	This work

Reference

1 Q. Q. Li, S. Li, D. Wu, Z. K. Ding, X. H. Cao, L. Huang, H. Pan, B. Li, K. Q. Chen, and X. D. Duan, *Appl. Phys. Lett.*, 2021, **119**, 162402, DOI: 10.1063/5.0068018

2 X. L. Sui, T. Hu, J. F. Wang, B. L. Gu, W. H. Duan, and M. S. Miao, *Phys. Rev. B*, 2017, **96**, 041410, DOI: 10.1103/PhysRevB.96.041410

3 J. J. Zhang, D. Zhu, and B. I. Yakobson, *Nano Lett.*, 2020, **21**, 785-790, DOI: 10.1021/acs.nanolett.0c04531

4 Z. Cui, B. Sa, K.-H. Xue, Y. Zhang, R. Xiong, C. Wen, X. Miao, and Z. Sun, *Nanoscale*, 2024, **16**, 1331-1344, DOI: 10.1039/d3nr04712a

5 Z. Yan, Z. Li, Y. Han, Z. Qiao, and X. Xu, *Phys. Rev. B*, 2022, **105**, 075423, DOI: 10.1103/PhysRevB.105.075423

6 R. Zhang, R. Jiao, Z. Fu, H. Yuan, J. He, L. Shen, X. Liao, Y. Zhou, and J. Yuan, *Phys. Rev. B*, 2025, **111**, 155414, DOI: 10.1103/PhysRevB.111.155414

7 L. Zhang, G. Ni, J. He, and G. Gao, *Phys. Rev. B*, 2025, **112**, 064401, DOI: 10.1103/j559-slg4

8 K. Klyukin, L. L. Tao, E. Y. Tsymbal, and V. Alexandrov, *Phys. Rev. Lett.*, 2018, **121**, 056601, DOI: 10.1103/PhysRevLett.121.056601

9 M. Zhou, X. Lu, Z. Wu, Y. Xie, Y. Xing, and Y. Wang, *Appl. Phys. Lett.*, 2021, **119**, 132903, DOI: 10.1063/5.0057877

10 Y. Su, X. Li, M. Zhu, J. Zhang, L. You, and E. Y. Tsymbal, *Nano Lett.*, 2020, **21**, 175-181, DOI: 10.1021/acs.nanolett.0c03452

11 Z. Cui, B. S. Sa, K. H. Xue, Y. G. Zhang, R. Xiong, C. L. Wen, X. S. Miao, and Z. M. Sun, *Nanoscale*, 2024, **16**, 1331-1344, DOI: 10.1039/d3nr04712a

12 W. Yang, Y. Xu, S. Li, J. Han, J. Chen, J.-C. Rojas-Sánchez, S. Mangin, X. Lin, and W. Zhao, *ACS Nano*, 2025, **19**, 38573-38582, DOI: 10.1021/acsnano.5c12783

13 Y. Zhu, B. Y. Chi, L. N. Jiang, X. Y. Guo, Y. Yan, and X. F. Han, *Phys. Rev. Appl.*, 2023, **20**, 034010, DOI: 10.1103/PhysRevApplied.20.034010

14 H. Bai, X. Li, H. Pan, P. He, Z.-a. Xu, and Y. Lu, *ACS Appl. Mater. Interfaces*, 2021, **13**, 60200-60208, DOI: 10.1021/acsami.1c18949

15 X. Dong, X. Shen, X. Sun, Y. Bai, Z. Yan, and X. Xu, *Phys. Rev. B*, 2023, **108**, 085427, DOI: 10.1103/PhysRevB.108.085427